



Article

# Enlarged Interlayer Spacing of Marigold-Shaped 1T-MoS<sub>2</sub> with Sulfur Vacancies via Oxygen-Assisted Phosphorus Embedding for Rechargeable Zinc-Ion Batteries

Qinhu Xu, Xinyu Li \*, Luchen Wu, Zhen Zhang, Yong Chen, Ling Liu and Yong Cheng \*

College of Science & Ministry-Province Jointly-Constructed Cultivation Base for State Key Laboratory of Processing for Mom-Ferrous Metal and Featured Materials & Key Lab. of Nonferrous Materials and New Processing Technology & Network and Information Center, Guilin University of Technology, Guilin 541004, China

\* Correspondence: lixinyu5260@163.com (X.L.); hb\_cy@163.com (Y.C.)

**Abstract:** Structural unsteadiness and sluggish diffusion of divalent zinc cations in cathodes during cycling severely limit further applications of MoS<sub>2</sub> for rechargeable aqueous zinc-ion batteries (ZIBs). To circumvent these hurdles, herein, phosphorus (P) atom embedded three-dimensional marigold-shaped 1T MoS<sub>2</sub> structures combined with the design of S vacancies (Sv) are synthesized via the oxygen-assisted solvent heat method. The oxygen-assisted method is utilized to aid the P-embedding into the MoS<sub>2</sub> crystal, which can expand the interlayer spacing of P-MoS<sub>2</sub> and strengthen Zn<sup>2+</sup> intercalation/deintercalation. Meanwhile, the three-dimensional marigold-shaped structure with 1T phase retains the internal free space, can adapt to the volume change during charge and discharge, and improve the overall conductivity. Moreover, Sv is not only conducive to the formation of rich active sites to diffuse electrons and Zn<sup>2+</sup> but also improves the storage capacity of Zn<sup>2+</sup>. The electrochemical results show that P-MoS<sub>2</sub> can reach a high specific capacity of 249 mAh g<sup>-1</sup> at 0.1 A g<sup>-1</sup>. The capacity remains at 102 mAh g<sup>-1</sup> after 3260 cycles at a current of 0.5 A g<sup>-1</sup>, showing excellent electrochemical performance for Zn<sup>2+</sup> ion storage. This research provides a more efficient method of P atom embedded MoS<sub>2</sub>-based electrodes and will heighten our comprehension of developing cathodes for the ZIBs.



**Citation:** Xu, Q.; Li, X.; Wu, L.; Zhang, Z.; Chen, Y.; Liu, L.; Cheng, Y. Enlarged Interlayer Spacing of Marigold-Shaped 1T-MoS<sub>2</sub> with Sulfur Vacancies via Oxygen-Assisted Phosphorus Embedding for Rechargeable Zinc-Ion Batteries. *Nanomaterials* **2023**, *13*, 1185. <https://doi.org/10.3390/nano13071185>

Academic Editors: Maiyong Zhu and Carlos Miguel Costa

Received: 26 February 2023

Revised: 22 March 2023

Accepted: 23 March 2023

Published: 27 March 2023



**Copyright:** © 2023 by the authors. Licensee MDPI, Basel, Switzerland. This article is an open access article distributed under the terms and conditions of the Creative Commons Attribution (CC BY) license (<https://creativecommons.org/licenses/by/4.0/>).

## 1. Introduction

Due to the distinct characteristics of zinc metal, such as high theoretical capacity (820 mAh g<sup>-1</sup>), low redox potential (-0.76 V concerning standard hydrogen electrodes), nontoxicity, low cost, and intrinsic safety, as well as high reversibility in aqueous electrolytes, ZIBs hold promising potential for large-scale energy storage [1–4]. However, Zn<sup>2+</sup> in aqueous solution is hard to intercalate between layers because it exists as hydrated zinc ions ([Zn(H<sub>2</sub>O)<sub>6</sub>]<sup>2+</sup>) with a size of 0.404 nm~0.43 nm, making ([Zn(H<sub>2</sub>O)<sub>6</sub>]<sup>2+</sup>) intercalation and deintercalation put forward higher requirements on the interlayer spacing and other properties of the cathode material [5–7]. In addition, divalent Zn<sup>2+</sup> usually exhibits strong electrostatic interactions with the host lattice, inhibiting the diffusion process of Zn<sup>2+</sup>, resulting in few cathode materials available for ZIBs, which are mainly confined to manganese-based materials, vanadium-based materials, and Prussian blue [8–10]. Therefore, the sluggish intercalation dynamics of divalent Zn<sup>2+</sup> enable the search for appropriate cathode materials to be very important for the development and application of ZIBs.

Molybdenum disulfide (MoS<sub>2</sub>) is a typical layered transition metal sulfide, and the covalently bonded S-Mo-S layers are stacked together by weak van der Waals forces, which is conducive to the intercalation of foreign guests [11–14]. Unfortunately, due to the strong electrostatic interaction between inserted Zn<sup>2+</sup> with a large hydrated radius (4.3 Å) and

host structures,  $Zn^{2+}$  is challenging to intercalate/deintercalate from the host frame, greatly affecting the reversible capability and rate characteristic of  $MoS_2$  as cathodes arousing from its smaller layer spacing and the large inert base with fewer active sites [15–18]. Moreover,  $MoS_2$  also has problems such as poor conductivity, poor hydrophilicity, agglomeration, and volume expansion, which limits the application of  $MoS_2$  in ZIBs. Therefore, some pioneering efforts, including introducing phase transition engineering and tailoring nanostructures, have been made to improve the  $Zn^{2+}$  storage capability of  $MoS_2$  cathodes [19–22]. One available strategy to resolve such challenges is to intercalate foreign elements into  $MoS_2$  to enlarge layer spacing [15,23,24]. Experimental and calculation results indicate that P dopants could not only modify the surface electronic state of  $MoS_2$  and increase its inherent conductivity but also lead to  $MoS_2$  expansion and induce a partial phase transition of  $MoS_2$  from hydrophobic (2H phase) to hydrophilic (1T phase); the 1T- $MoS_2$  has lower  $Zn$  diffusion energy barriers [25]. However, due to the spontaneous formation of  $MoP$ , resulting in P atom doping is inherently difficult and has lower P content [26,27]. Despite substantial achievements having been made, P-embedding 1T- $MoS_2$  to achieve extended layer spacing for enhancing the ability of  $Zn^{2+}$  intercalates/deintercalates is very necessary, thus requiring a facile method.

Additionally, vacancy engineering has been in the spotlight as a feasible strategy to enhance the zinc ions storage capability considerably. Especially based on previous reports [28], sulfur vacancies can provide abundant active sites as additional ion storage sites for  $Zn^{2+}$  as well as offer a fast electrochemical response. For example, Hu et al. [29] developed a few-layered  $MoS_2$  anchored on an N-doped carbon flower with Sv as anode material for sodium-ion batteries, exhibiting excellent performance. Wang et al. [30] improved the performance of hydrogen evolution reaction (HER) by regulating the S-vacancy distribution and concentration in  $MoS_2$ . Xu et al. reported that the preparation of defect-rich  $MoS_2$  accelerated the diffusion kinetics of  $Zn^{2+}$  to the active center [31]. Therefore, the rational S vacancy modulation strategy is essential to improve the reaction kinetics of  $Zn^{2+}$  for realizing its application in ZIBs.

Herein, an oxygen-assisted(O) strategy is used to aid the P-embedding into the  $MoS_2$  crystal; the  $MoS_2$  layer spacing is expanded, and the marigold-shaped 1T- $MoS_2$  nanosheets with rich S vacancies are prepared. In this process, oxygen played a key role in aiding the successful embedding of P into the lattice of 1T- $MoS_2$ . The intercalation of P in  $MoS_2$  achieves the desired effect, significantly enlarging  $MoS_2$  interlayers (from 0.62 to 0.98 nm) and enhancing hydrophilicity. In addition, these S vacancies defects as active sites can make it easier for  $Zn^{2+}$  adsorption and desorption. The synergistic effect of P-embedding induced and extended the marigold-shaped 1T- $MoS_2$  layer spacing and caused the Sv to form an active center in the basal plane of  $MoS_2$ , effectively reducing the  $Zn^{2+}$  diffusion resistance. It provides an easier channel for the insertion of  $[Zn(H_2O)_6]^{2+}$ , resulting in rapid reaction kinetics. As expected, the P- $MoS_2$  electrode achieves a remarkably high capability of  $249\text{ mAh g}^{-1}$  at  $0.1\text{ A g}^{-1}$ , which is five times higher than the specific capacity of pristine  $MoS_2$ . In comparison to the pristine P- $MoS_2$  counterpart with minimal capacity delivery, P- $MoS_2$  can achieve a high reversible capacity of  $105\text{ mAh g}^{-1}$  at  $0.5\text{ A g}^{-1}$  with 3260 cycles and excellent capacity retention of  $70\text{ mAh g}^{-1}$  at  $1\text{ A g}^{-1}$ . This study will provide more efficient avenues for investigating more electrode materials with poor intercalation kinetics in ZIBs.

## 2. Methods

### 2.1. Experimental Section

Synthesis of P- $MoS_2$ : In a representative procedure, 1 mmol (1236 mg) ammonium molybdate tetrahydrate ( $(NH_4)_6Mo_7O_{24}\cdot 4H_2O$ , AR) and 30 mmol (2284 mg) thiourea ( $CH_4N_2S$ , AR) were added into 35 mL deionized water on the basis of a beforehand report with slight adjustment [32]. After being stirred for 30 min, an amount of sodium hypophosphite monohydrate ( $NaH_2PO_2\cdot 4H_2O$ , AR, 400 mg) was dissolved into a mixed solution with magnetic stirring for 2 h. Then, the precursor solution was heated to  $180^\circ C$

for 24 h in a 50 mL Teflon-lined stainless steel autoclave. After cooling the reaction system to air temperature, which was collected by centrifugation, cleaned multiple times with water, and then dried at 80 °C. As a contrast, pristine MoS<sub>2</sub> was also prepared without NaH<sub>2</sub>PO<sub>2</sub>·4H<sub>2</sub>O following a similar synthetic route.

## 2.2. Material Characterizations

The morphology of materials was evaluated with a scanning electron microscope (SEM, Hitachi S-4800, Tokyo, Japan) and a transmission electron microscope (TEM, Tecnai G2 20 TWIN, FEI, Hillsboro, OR, USA). An energy dispersive spectrometer (EDS S-00123, USA) connected to the SEM was used to study the elemental composition and elemental analyses of the composites. At −196 °C, N<sub>2</sub> adsorption/desorption isotherms were measured with an automated SSA and porosity analyzer (asap2460). Brunauer–Emmett–Teller (BET) and Barrett–Joyner–Halenda (BJH) adsorption techniques were used to determine the SSA and mesopore size distribution of each sample. All samples' crystal phases and compositions were determined using X-ray diffraction (XRD, MiniFlex-600, Rigaku, Tokyo, Japan) and X-ray photoelectron spectroscopy (XPS, Thermo Scientific K-Alpha, Waltham, MA, USA). Raman spectra at 532 nm were measured with a Horiba Scientific LabRAM HR Evolution Raman spectrometer. The TGA/DTA was tested by thermogravimetric analysis equipment (SDT Q600, USA) from room temperature to 750 °C at a heating rate of 10 °C/min. A hydrophilicity test was measured using a contact angle test device (Dataphysics OCA20, Filderstadt, Germany).

## 2.3. Electrochemical Characterization

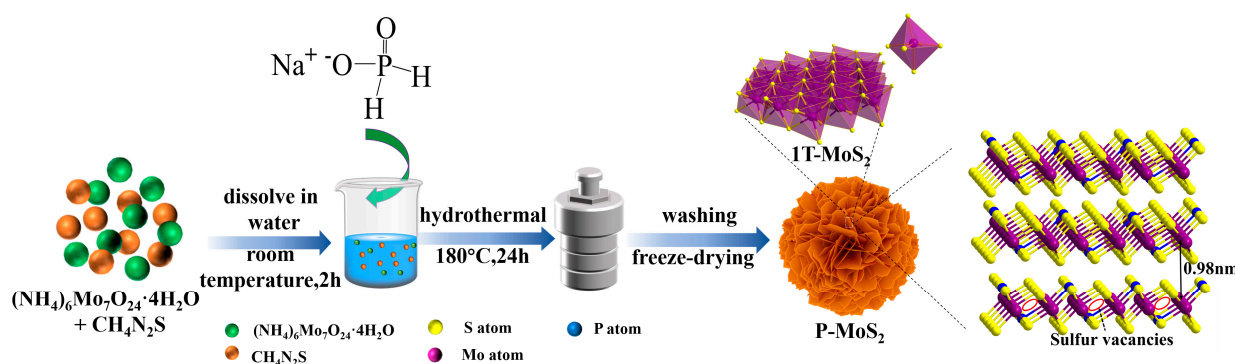
Zn served as the anode, glass fiber membrane served as diaphragms, and 3 M Zn(CF<sub>3</sub>SO<sub>3</sub>)<sub>2</sub> served as the electrolyte in CR2016-type coin cells used to investigate the Zn<sup>2+</sup> storage properties of P-MoS<sub>2</sub>. To manufacture the working electrode, P-MoS<sub>2</sub> (70 weight percent), super p carbon (20 weight percent), and polyvinylidene fluoride (10 weight percent) were thoroughly blended in *N*-methyl-2-pyrrolidone for 15 min. Finally, the aforementioned slurry was distributed over a clean stainless steel mesh and dried for 24 h at 60 °C. On a Neware battery tester (CT4008), galvanostatic charge/discharge measurements and galvanostatic intermittent titration technique (GITT) experiments were carried out continuously between 0.25 and 1.25 V (vs. Zn/Zn<sup>2+</sup>). An electrochemical workstation was used for the cyclic voltammetry (CV) and electrochemical impedance spectroscopy (EIS) experiments (CHI-660D). When the batteries were completely charged, impedance measurements were taken (zinc extraction). At room temperature, all tests were conducted dw.

## 3. Results and Discussion

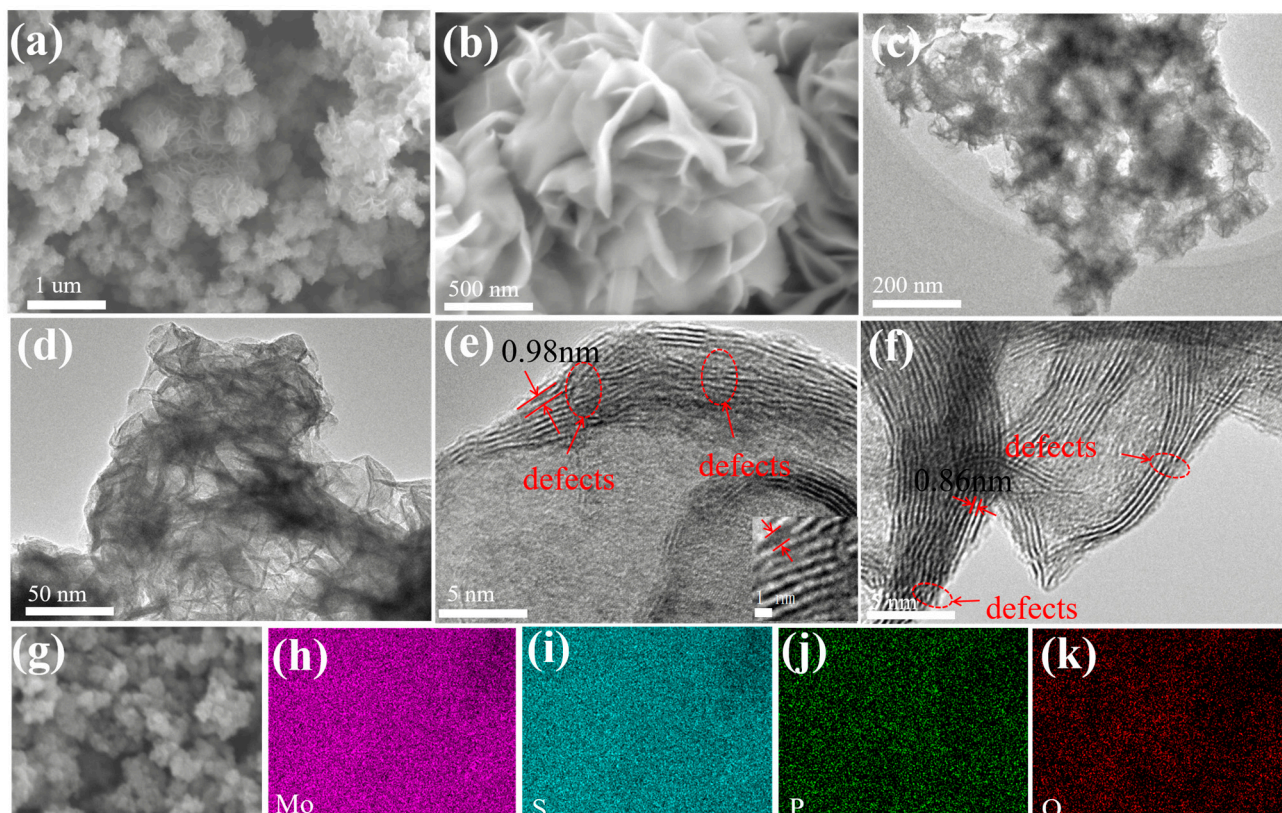
### 3.1. Composition and Structure

Figure 1 depicts the synthesis process of P-MoS<sub>2</sub> and pristine MoS<sub>2</sub>. The phosphorus embedded three-dimensional marigold 1T MoS<sub>2</sub> was obtained by controlling the crystallization process. In a nutshell, an oxygen-rich atmosphere plays a vital role in decreasing the formation energy of P-embedding in MoS<sub>2</sub> [26]. The reaction process becomes more inadequate as the synthesis temperature decreases, resulting in the leftover oxygen inherited from the molybdate precursor, thus realizing the oxygen-rich atmosphere [32]. Additionally, most of the Mo<sup>4+</sup> ions form ionic bonds with S<sup>2−</sup>, which are self-assembled in the form of nanocrystals connected into three-dimensional marigold-shaped structures. Excess thiourea could be adsorbed on the surfaces of initial nanocrystallites and impede the formation of orientated crystals, which results in abundant Sv being produced amid the flat structure [33]. The SEM and TEM were utilized to explore the morphology evolution of as-prepared P-MoS<sub>2</sub> further. As shown in Figure 2a,b, the SEM of P-MoS<sub>2</sub> displays the magnificent marigold structure with an internal diameter of almost 1 μm, which was self-assembled from curved thickness nanosheets with transverse dimensions of 400–500 nm. In comparison, pristine MoS<sub>2</sub> has a rather formidable nanosheet microstructure, which is much larger in transverse size (diameter almost 4–5 μm) and displays severe aggregation

in the absence of a well-tuned morphology (Figure S1). The relatively smaller size of the beautiful marigold structure should help to shorten the  $Zn^{2+}$  diffusion duration. The uneven nanostructure of P-MoS<sub>2</sub> with evident ripples and bending wrinkles is depicted in TEM images (Figure 2c,d), in which nanosheets are haphazardly joined and formed into three-dimensional structures. The TEM images in Figure 1e,f reveal a distinct lattice structure with some disorder and abundance of Sv (Figure S2), resulting in an incomplete lattice that may accommodate a host of unsaturated S atoms as active sites. Furthermore, the TEM images reveal that dozens of pristine MoS<sub>2</sub> layers are heavily stacked together with an interlayer spacing of 0.62 nm (Figure S3), whereas the stacking of the P-MoS<sub>2</sub> layers is significantly relieved with the interlayer distance strikingly expanding to 0.98 nm (Figure S4) and 0.86 nm. The results show that P-embedding can enlarge the layer spacing of P-MoS<sub>2</sub>, which is advantageous to strengthen  $Zn^{2+}$  intercalates/deintercalates. Figure 2h–k displays the mapping images of P-MoS<sub>2</sub>, which expressly demonstrate that Mo, O, S, and P elements are distributed uniformly. Meanwhile, Figure S5 shows the elemental content of P-MoS<sub>2</sub>.



**Figure 1.** Schematic illustration of synthesis P-MoS<sub>2</sub>.



**Figure 2.** (a,b) SEM; (c,d) TEM; (e,f) HRTEM; (g–k) EDS of P-MoS<sub>2</sub>.

The structural information of the two obtained samples was studied by X-ray diffraction (XRD) analysis (Figure 3a). Compared with the highly crystalline pristine MoS<sub>2</sub> in the 2H-MoS<sub>2</sub> phase (JCPDS card number 37–1492), all peaks of the P-MoS<sub>2</sub> are broadened due to nanoscale effects and crystal structural defects. The weakening of the (002) diffraction peak of P-MoS<sub>2</sub> indicates a low stacking height along this direction [34,35]. Meanwhile, the (002) peak of P-MoS<sub>2</sub> slightly shifts to a lower angle ( $14.2^\circ \rightarrow 13.96^\circ$ ), indicating the formation of sulfur vacancies in MoS<sub>2</sub> [36,37]. In addition, a new peak appeared at  $9.8^\circ$ , which is related to the presence of P, leading to the formation of a stacking layer, thus extending the c-axis of MoS<sub>2</sub>. According to Bragg's law, the lattice spacing of the stacking layer at  $9.8^\circ$  is consistent with the spacing in TEM. Due to P's larger atomic radius than S, P atoms were introduced into the MoS<sub>2</sub> matrix, causing the lattice to expand and contributing to the widening of interlayer spacing [25,38,39]. Figure 3b exhibits the Raman spectra of P-MoS<sub>2</sub>. Three typical Raman scattering peaks at  $280\text{ cm}^{-1}$  ( $E_{1g}^1$ ),  $234\text{ cm}^{-1}$  ( $J_2$ ), and  $334\text{ cm}^{-1}$  ( $J_3$ ) are attributed to the octahedral coordination of metal 1T-MoS<sub>2</sub> [40–42]. P-MoS<sub>2</sub> exhibits two typical characteristic peaks at  $376\text{ cm}^{-1}$  and  $394\text{ cm}^{-1}$ , corresponding to the in-plane ( $E_{2g}^1$ ) and out-of-plane ( $A_{1g}$ ) modes of 2H MoS<sub>2</sub>, which are clearly distinct from pristine MoS<sub>2</sub>. The distance between the  $E_{2g}^1$  and  $A_{1g}$  peaks is  $18\text{ cm}^{-1}$  for P-MoS<sub>2</sub> and  $23\text{ cm}^{-1}$  for bulk MoS<sub>2</sub>. Thus, the moving peak of  $A_{1g}$  might represent the substantial out-of-plane vibration, indicating that the decreased van der Waals force, together with the enlarged interlayer spacing of MoS<sub>2</sub> caused by P-embedding, is favourable for Zn<sup>2+</sup> movement and storage [5,43]. The weaker intensity of the  $E_{2g}^1$  peak in P-MoS<sub>2</sub> is weaker compared to other samples, thereby proving the presence of S<sub>v</sub> in the crystal structure [44].

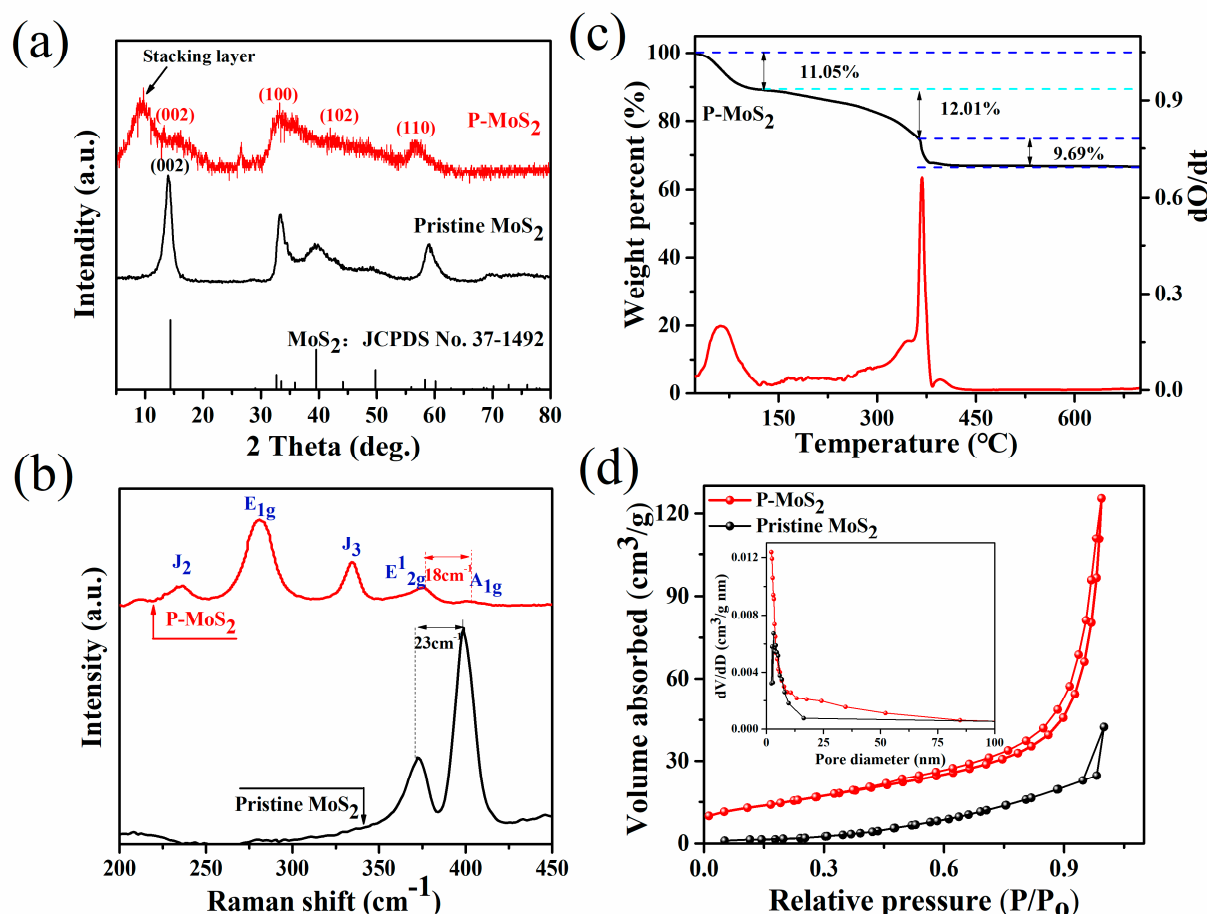


**Figure 3.** (a) XRD patterns of P-MoS<sub>2</sub> and pristine P-MoS<sub>2</sub>. (b) Raman spectra of P-MoS<sub>2</sub> and pristine MoS<sub>2</sub>. (c) TGA and DTA curves of P-MoS<sub>2</sub>. (d)  $N_2$  adsorption/desorption isotherm and corresponding pore size distribution of P-MoS<sub>2</sub> and pristine MoS<sub>2</sub>.

The TGA-DTA results for the P-MoS<sub>2</sub> shown in Figure 3c show the initial mass loss of 11.05 wt% at 135 °C due to surface-adsorbed water evaporation. The mass loss of 12.01 wt% between 135 and 350 °C corresponds to the water loss integrated into the crystal structure, implying that the enlarged layer spacing of P-MoS<sub>2</sub> is probably caused by water insertion [45]. The additional weight loss of 9.69% over 350 °C may be caused by O atoms, which are utilized to aid P atoms embedded in the MoS<sub>2</sub> structure, with the unsaturated S atoms resulting in the reaction  $2\text{MoS}_2 + 7\text{O}_2 \rightarrow 2\text{MoO}_3 + 4\text{SO}_2$  [46,47]. The first derivative curve of the related DTA curve shows a visible endothermic peak at 350 °C. This peak is caused by the transformation of the crystal structure of MoS<sub>2</sub>, which is confirmed by XRD analysis. Moreover, the cumulative pore volume and BET surface area of P-MoS<sub>2</sub> and pristine MoS<sub>2</sub> were also measured. As shown in Figure 3d, P-MoS<sub>2</sub> and pristine MoS<sub>2</sub> exhibited typical type IV isotherms with hysteresis loops, indicating mesopores between MoS<sub>2</sub> nanosheets. Nevertheless, the hysteresis of P-MoS<sub>2</sub> starts at a lower pressure region ( $P/P_0 \approx 0.5$ ) than that of pristine MoS<sub>2</sub> ( $P/P_0 \approx 1$ ), showing their different porous nature. Furthermore, the wide hysteresis of P-MoS<sub>2</sub> indicates its increase in porosity. According to the pore volume–pore size distribution curve, P-MoS<sub>2</sub> has more abundant mesoporous structures, which is conducive to electron transport. The increased specific surface area of P-MoS<sub>2</sub> is 51.572 m<sup>2</sup> g<sup>-1</sup>, which is significantly more than pristine MoS<sub>2</sub> (11 m<sup>2</sup> g<sup>-1</sup>). The increased specific surface area improves the interaction between the material's exposed active sites and the electrolyte, which favors increasing the number of active sites for Zn<sup>2+</sup> storage. These results clearly show that the P-embedding strategy can greatly increase the surface area and pore volume of MoS<sub>2</sub>. To evaluate the hydrophilicity of P-MoS<sub>2</sub>, we performed a contact angle test. Water contact angles of P-MoS<sub>2</sub> drop from 54.46° to 38.8° (Figure S6), suggesting improved hydrophilicity and beneficial to the diffusion of Zn<sup>2+</sup> [6].

X-ray photoelectron spectroscopy (XPS) reveals detailed valence states and chemical contents of manufactured materials. The survey XPS spectra for P-MoS<sub>2</sub> and is displayed in Figure S7. As shown in Figure 4a, the XPS spectra of the Mo 3d scan contain two sets of doublet peaks (228.55 and 231.76 eV; 229.5 and 232.75 eV), which belong to Mo 3d<sub>5/2</sub> and Mo 3d<sub>3/2</sub> of Mo<sup>4+</sup> for 1T-MoS<sub>2</sub> and 2H-MoS<sub>2</sub> [19,48,49]. This suggests the coexistence of 2H and 1T in P-MoS<sub>2</sub>, which is compatible with Raman data. Similarly, differences can be observed in the S 2p spectra in Figure 4b, where peaks at 161.4 (S 3d<sub>3/2</sub> of S<sup>2-</sup>) and 162.7 eV (S 3d<sub>1/2</sub> of S<sup>2-</sup>) attributed to 1T MoS<sub>2</sub>, while peaks at 162.0 and 163.1 eV ascribed to 2H-MoS<sub>2</sub> [49]. After fitting S 2p spectrum, an extra peak can be seen at 164.19 eV, according to the relevant literature, ascribed to the edge S [50]. Furthermore, using deconvolutions of Mo 3d, the proportion of 1T is estimated at 53% (Table S1), which is equivalent to the product obtained from chemical exfoliation [21]. Meanwhile, the existence of the O 1s signal offers conclusive proof of oxygen-assisted P-embedding in P-MoS<sub>2</sub> (Figure 4c). It can be deconvoluted into three peaks at 530.42, 531.94, and 533.44 eV, which is ascribed to the P-O bond, Mo-O bond, and adsorbed water, respectively. The analysis shows that oxygen plays an auxiliary role in P-embedding and can also make P-MoS<sub>2</sub> form a three-dimensional beautiful marigold structure in a bonding manner. P 2p signals were detected at 134.02, 130.99, and 130.06 eV (Figure 4d), confirming the existence of P. The dominant P signal at 134.6 eV can be allocated to the PO<sub>4</sub><sup>3-</sup> species, whereas the remaining two should be attributed to Mo-P, indicating that P atoms are embedded in the MoS<sub>2</sub> lattice [44,51]. Furthermore, elemental composition analysis reveals that the Mo/S ratio is around 1:1.73 (Table S2), which is much lower than the 1:1.95 for MoS<sub>2</sub> by XPS. This finding implies that P-MoS<sub>2</sub> has a substantial number of S vacancies [5,20,45].

### 3.2. Electrochemical Performance of Aqueous Zn-Ion Batteries and Kinetic

To investigate the Zn<sup>2+</sup> storage capacity of the prepared samples as stand-alone cathodes for AZIBs, CR2016 coin cells were manufactured in the air environment (see the experimental section for details). Cyclic voltammetry (CV) curves in a voltage window of 0.25 to 1.25 V of 0.1 mV s<sup>-1</sup> are shown in Figure 5a,b. In contrast to pristine MoS<sub>2</sub>, P-MoS<sub>2</sub> has two redox peaks: the cathodic peak at 0.65 V linked to Zn<sup>2+</sup> insertion (possibly

overlapping or merging with the reduction in  $\text{Mo}^{6+}/\text{Mo}^{4+}$ ) and an anodic peak at 0.98 V is associated to  $\text{Zn}^{2+}$  inlay removal [23]. Furthermore, the second and third CV cycles of the two electrodes practically coincide, showing high reversibility. Surprisingly, the peak area of P-MoS<sub>2</sub> is considerably larger than that of pristine MoS<sub>2</sub>, showing that the enlarged layer spacing and  $\text{Sv}$  can significantly boost volume capacity. The P-MoS<sub>2</sub> charge/discharge (CD) curves are comparable with the CV data (Figure 5c), which shows an intercalation plateau of P-MoS<sub>2</sub> approximately 0.6 V. In addition, the specific capacity of P-MoS<sub>2</sub> is 249  $\text{mA h g}^{-1}$ , which is more than five times that of pristine MoS<sub>2</sub> (50  $\text{mA h g}^{-1}$ ), significantly better than the well-known  $\text{Zn}^{2+}$  intercalation host, i.e., the Chevrel Phase Mo<sub>6</sub>S<sub>8</sub> (60  $\text{mA h g}^{-1}$  at 0.06  $\text{A g}^{-1}$ ) [52,53]. Meanwhile, the capacity of several modified MoS<sub>2</sub> materials is compared at 0.1  $\text{A g}^{-1}$  in Table S3. Figure 5d shows display ratio capability with the volumes of P-MoS<sub>2</sub>, which are 249, 158, 125, 97, and 75  $\text{mAh g}^{-1}$  at 0.1, 0.2, 0.5, 1, and 2  $\text{A g}^{-1}$ , respectively, and Figure 5e shows the charge/discharge curves of the first cycle capacity. P-MoS<sub>2</sub> capacitance achieves 143  $\text{mAh g}^{-1}$  (91% capacity retention) when it reaches 0.2  $\text{A g}^{-1}$ . These hint at the excellent rate characteristic and rapid dynamics of P-MoS<sub>2</sub>. In contrast, pristine MoS<sub>2</sub> offers rather low capacities (0–45  $\text{mAh g}^{-1}$ ) at a variety of current densities. P-MoS<sub>2</sub> demonstrates a consistent capacity of 70  $\text{mAh g}^{-1}$  after 200 cycles at 1  $\text{A g}^{-1}$  to further illustrate its outstanding working life (Figure 5f). The stability was further investigated at 0.5  $\text{A g}^{-1}$  in Figure 5g.

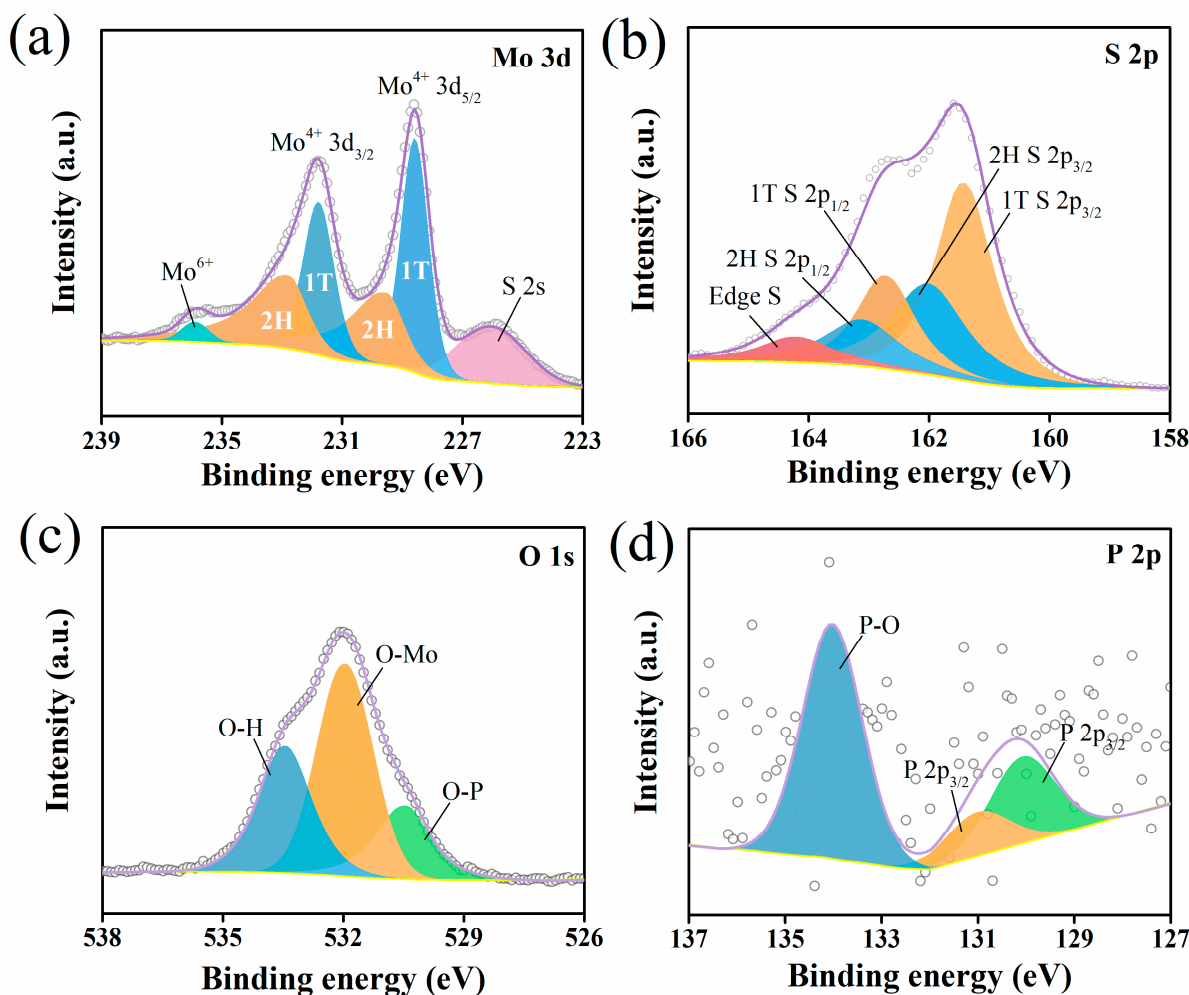


**Figure 4.** XPS spectra of P-MoS<sub>2</sub>: (a) Mo 3d, (b) S 2p, (c) O 1s, and (d) P 2p.

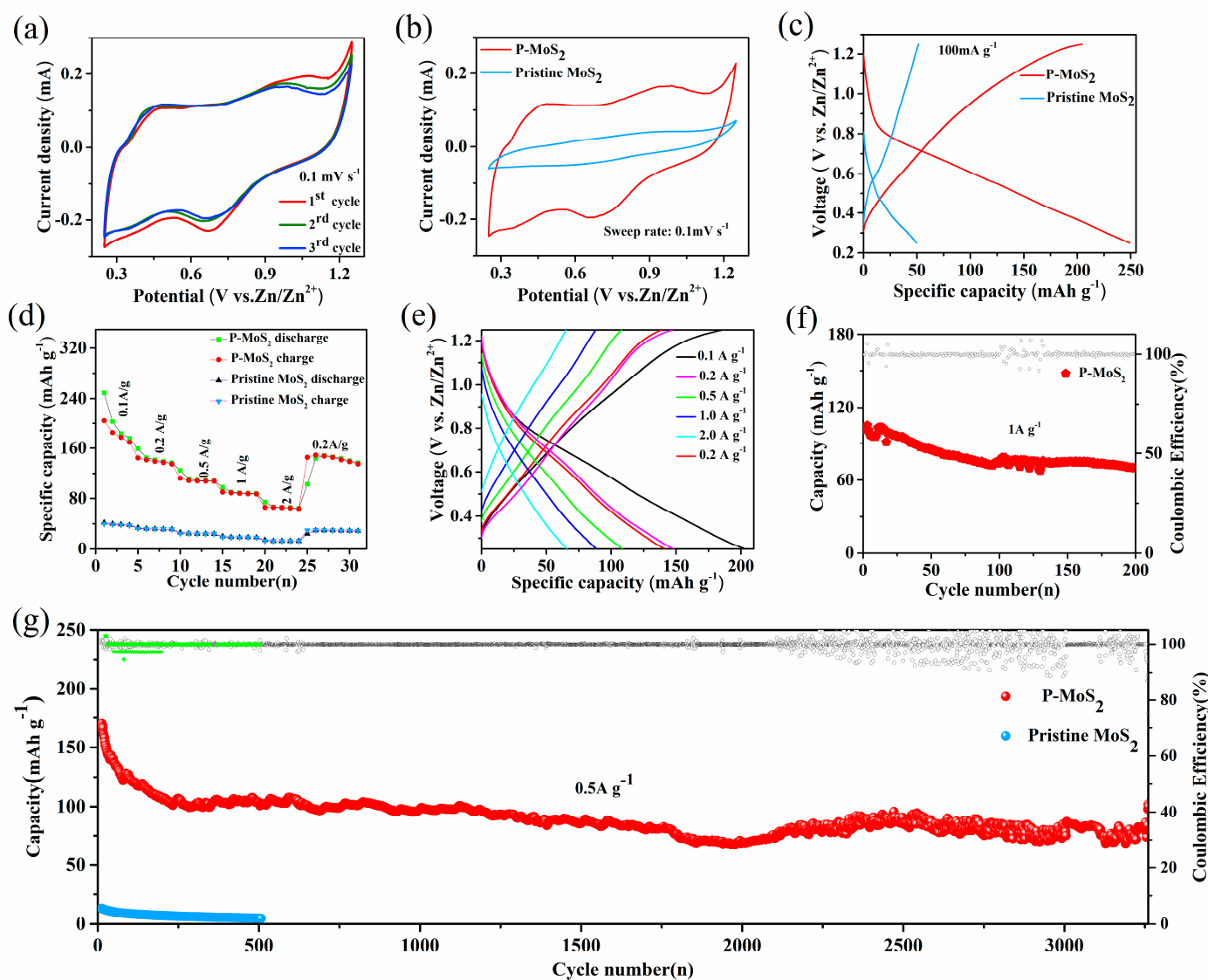


**Figure 5.** Electrochemical performance of P-MoS<sub>2</sub> and pristine MoS<sub>2</sub> **(a)** CV curves at  $0.1 \text{ mV s}^{-1}$ . **(b)** CV at  $0.1 \text{ mV s}^{-1}$  rate of P-MoS<sub>2</sub> and Pristine MoS<sub>2</sub>. **(c)** Discharge/charge curves at  $0.1 \text{ A g}^{-1}$ . **(d)** Rate performance. **(e)** First cycle capacity at different cycles. **(f)** Two hundred cycling stability at  $1 \text{ A g}^{-1}$ . **(g)** Long-term cycling stability at  $0.5 \text{ A g}^{-1}$ .

P-MoS<sub>2</sub> maintains a capacity of  $102 \text{ mAh g}^{-1}$  after 3260 cycles, achieving capacity retention of 70%, with the efficiency of the electrode being close to 100%. However, the cycling stability of the P-MoS<sub>2</sub> electrode seems rather poor after 2000 cycles, which is attributed to the irreversible structural damage, volume changes, and unstable 1T phase during the continuous charging and discharging process [54,55]. In comparison, pristine MoS<sub>2</sub> has almost zero capacity, which is related to its poor conductivity and unstable structure [16,23].

The results show that P-MoS<sub>2</sub> outperforms pristine MoS<sub>2</sub> in terms of reversible capacity, cycle stability, and rate capacity. To better understand the electrochemical reaction behavior of the P-MoS<sub>2</sub> electrode, CV curves at varied scan speeds ( $0.1\text{--}1.0 \text{ mV s}^{-1}$ ) are tested (Figures 6a and S8). The oxidation peak gradually shifted toward high potential with an increasing scan rate, and the reduction peak shifted toward low potential because the

electrode polarization broadened at a high scan rate. Whether pseudocapacitive behavior is present or absent depends on the kinetic equation of the reaction:

$$i = av^b \quad (1)$$

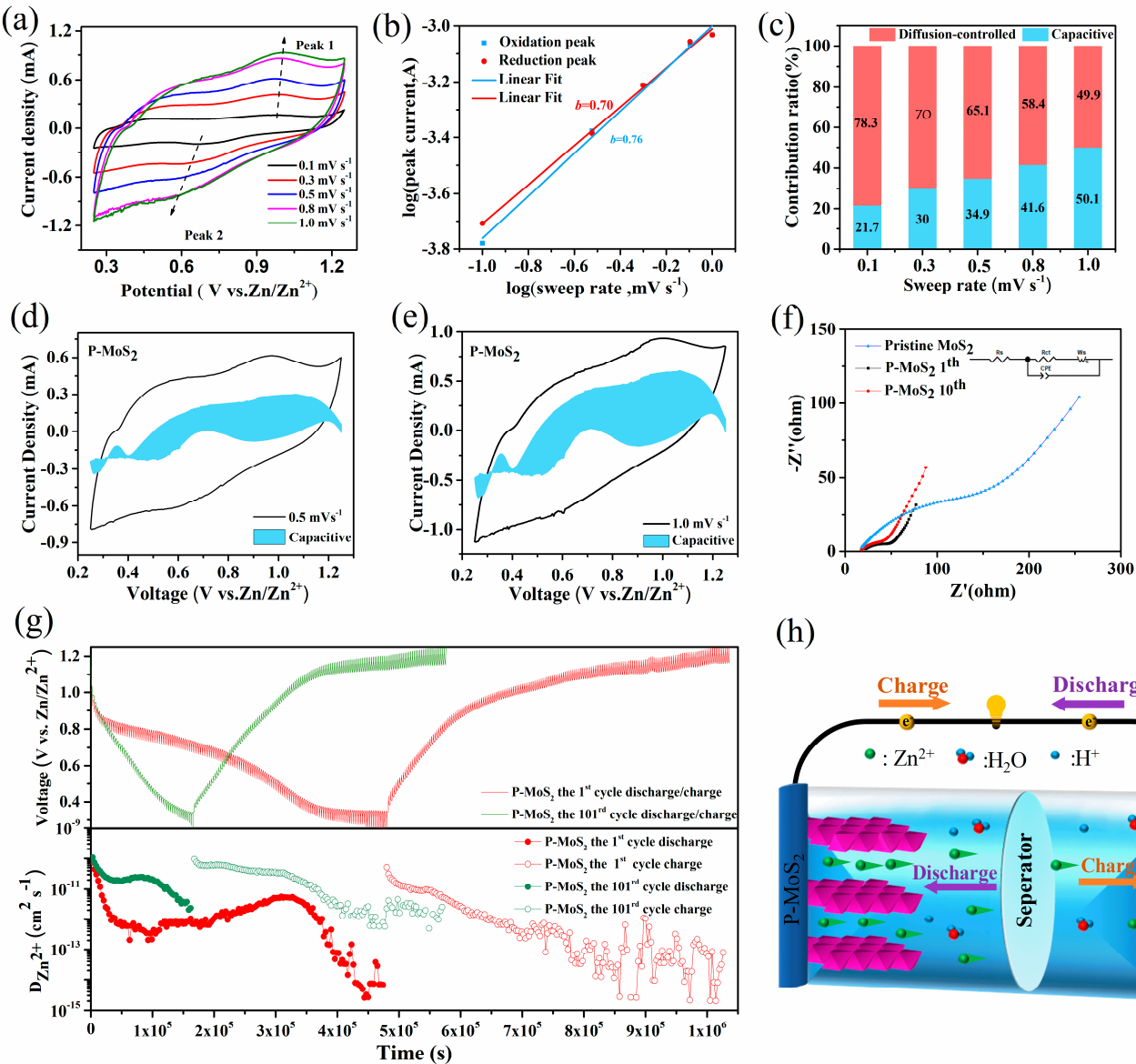


**Figure 6.** Electrochemical kinetics characterization for the P-MoS<sub>2</sub> electrode. (a) CV curves at various scan rates. (b) Log (*i*) versus log (*v*) plots of the redox peaks corresponding to the CV data. (c) Capacitive separation curves at 0.5 mV s<sup>-1</sup> (d) Capacitive separation curves at 0.5 mV s<sup>-1</sup>. (e) Capacitive separation curves at 1 mV s<sup>-1</sup>. (f) EIS spectra, insert image is the fitted equivalent circuit models. (g) Discharge/charge GITT profiles and corresponding D<sub>Zn</sub>. (h) Schematic diagram for Zn-storage mechanism of P-MoS<sub>2</sub>.

In between, *i* is the peak current, the unit is A, *v* is the sweep speed, the unit is mV/s, *a* and *b* are the adjustment parameters, and *b* is the slope value of the log (*i*) vs. log (*v*) graph. In particular, *b* = 0.5 indicates that the discharge-specific capacity belongs to the diffusion process control, and *b* = 1 implies the pseudocapacitance control. When *b* is between 0.5–1, there is both diffusion and pseudocapacitance behavior [56]. Obviously, Figure 6b indicates the *b*-values of peak 1 and peak 2, which are 0.76 and 0.70, showing that the redox reaction of the P-MoS<sub>2</sub> electrode consists of diffusion and capacitive processes. Additionally, the

capacitive contribution and diffusion contributions of P-MoS<sub>2</sub> may be evaluated based on the equation proposed by Dunn [57,58]:

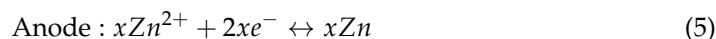
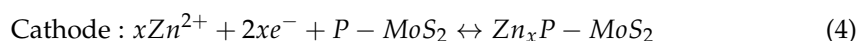
$$i(V) = k_1 v + k_2 v^{1/2} \quad (2)$$

$$i(V)/v^{1/2} = k_1 v^{1/2} \quad (3)$$

At a certain voltage ( $v$ ),  $i$  is the total current response, where  $k_2 v^{1/2}$  and  $k_1 v$  are diffusion-controlled and capacitance-dominated contributions. Figure 6c–e reveals the respective contribution rates at different scan rates. Notably, the capacitive contribution increases from 21.7% at 0.1 mV s<sup>-1</sup> to 50.1% at 1 mV s<sup>-1</sup>. The pseudocapacitance effect is slowly dominant, indicating that the surface reaction is faster than the internal diffusion reaction, which accelerates the intercalation and extraction of Zn<sup>2+</sup> in the material. Moreover, the diffusion characteristics of P-MoS<sub>2</sub> are more obvious, which can be attributed to the marigold-shaped structure and wide layer spacing [59]. The impedance of P-MoS<sub>2</sub> and pristine MoS<sub>2</sub> is evaluated by EIS, as shown in Figure 6f. The magnitude of the charge transfer resistance is reflected in the semicircle radius of the high-frequency zone (R<sub>ct</sub>, Table S4). Clearly, results show that the charge transfer impedance of P-MoS<sub>2</sub> is measured at 42.82 Ω, which is lower than the pristine MoS<sub>2</sub> under the same conditions. In addition, R<sub>ct</sub>s of pristine MoS<sub>2</sub> are markedly over 180 Ω, indicating that expanded layer spacing and S vacancies improve charge-transfer dynamics. Because of the activation of the active material, the charge transfer impedance of P-MoS<sub>2</sub> was lowered during the first ten cycles.

To examine the solid-state diffusion kinetics of Zn<sup>2+</sup> intercalation in P-MoS<sub>2</sub>, we investigated GITT, which has been widely used to assess ionic diffusivity, offering insight into electrode kinetics. Figure 6g shows the GITT of P-MoS<sub>2</sub> before and after 100 cycles, respectively; obviously the P-MoS<sub>2</sub> cell mainly provides a low Zn<sup>2+</sup> diffusion coefficient of around 10<sup>-15</sup>–10<sup>-10</sup> cm<sup>2</sup> s<sup>-1</sup> at the 1st cycle. After 100 cycles, the diffusion coefficient stability was increased to 10<sup>-12</sup>–10<sup>-10</sup> cm<sup>2</sup> s<sup>-1</sup>, which is attributed to the activation of the electrode and the opening of ion channels during the numerous discharging/charging progress [60,61]. The above electrochemical analysis shows that the Zn<sup>2+</sup> insertion kinetics of P-MoS<sub>2</sub> is accelerated, leading to a higher specific capacity. When the P atoms are embedded in the MoS<sub>2</sub> lattice, the expanded layer spacing of MoS<sub>2</sub> allows for easy Zn<sup>2+</sup> desorption. In addition, the P-embedding induces 1T-MoS<sub>2</sub> and abundant sulfur vacancies.

The material has excellent electrical conductivity and facilitates electron transfer. In addition, P-MoS<sub>2</sub> possesses a large amount of interlayer water and substantially increased hydrophilicity. As demonstrated in previous studies, interlayer water can act as an electrostatic shield, weakening the interaction of Zn<sup>2+</sup> with the host material's framework, lowering the diffusion energy barrier, and accelerating the migration efficiency of Zn<sup>2+</sup> [62,63]. Benefiting from these synergistic effects, P-MoS<sub>2</sub> exhibits satisfactory performance. On the basis of the aforementioned tests and analysis, the electrochemical mechanism of P-MoS<sub>2</sub> proposed in Figure 6h is shown, and the various electrochemical reactions that may occur with P-MoS<sub>2</sub> and Zn are classified as the following:



where  $x$  is the Zn<sup>2+</sup> content per unit of P-MoS<sub>2</sub> in the insertion state. Figure S9 shows that the Faraday equation may calculate 0.65 Zn<sup>2+</sup> per unit based on the discharge curve at 100 mA g<sup>-1</sup>. Furthermore, 0.65 Zn<sup>2+</sup> per unit was removed from the P-MoS<sub>2</sub> during the charging procedure.

#### 4. Conclusions

In summary, marigold-shaped 1T-MoS<sub>2</sub> material with rich S vacancy and expanded interlayer spacing to 0.98 nm was fabricated via the oxygen-assisted method, which found the 1T phase content (53%) and extensively analyzed their performance as cathode materials

for ZIBs. Meanwhile, the electrochemical investigation revealed that the S vacancy and interlayer spacing generated by P-embedding are particularly advantageous to the rapid diffusion of  $Zn^{2+}$  in P-MoS<sub>2</sub> and boost the  $Zn^{2+}$  storage capacity of the marigold-shaped nanosheets. In comparison to the pure MoS<sub>2</sub> equivalent, P-MoS<sub>2</sub> nanosheets have a great specific capacity and display outstanding continuous cycle capabilities in ZIBs. When the current density is  $0.1 \text{ A g}^{-1}$ , the discharge capacity can reach  $249 \text{ mAh g}^{-1}$ . In particular, it displayed a high specific discharge capacity of  $105 \text{ mAh g}^{-1}$  with a capacity retention of 70% after 3260 cycles at the current density of  $0.5 \text{ A g}^{-1}$  and an excellent capacity retention of  $70 \text{ mAh g}^{-1}$  at  $1 \text{ A g}^{-1}$ . This work offers new ideas for designing MoS<sub>2</sub> as cathode materials for ZIBs.

**Supplementary Materials:** The following supporting information can be downloaded at: <https://www.mdpi.com/article/10.3390/nano13071185/s1>. Figure S1. SEM images of the sample of Pristine MoS<sub>2</sub>; Figure S2. The corresponding atomic intensity profile along the dotted red line for P-MoS<sub>2</sub>; Figure S3. TEM images of (a,b) Pristine MoS<sub>2</sub>; Figure S4. Line scan of the HRTEM image; Figure S5. EDS spectrum; Figure S6. Contact angles with water for (a) P-MoS<sub>2</sub> and (b) Pristine MoS<sub>2</sub>; Figure S7. XPS spectra of full scan for P-MoS<sub>2</sub>; Figure S8. The initial five CV curves of (a) Pristine MoS<sub>2</sub> and (b) CV curves at various scan rates of Pristine MoS<sub>2</sub>; Figure S9. Initial charge-discharge profile of P-MoS<sub>2</sub> nanosheets at  $0.1 \text{ A g}^{-1}$ ; Table S1. Phase content of Mo 3d in each sample; Table S2. Atomic percentages of P-MoS<sub>2</sub> by XPS measurement; Table S3. Comparisons of performance of MoS<sub>2</sub> synthesized under different conditions in neutral media; Table S4. Charge transfer resistance of MoS<sub>2</sub> samples. References [64,65] are cited in Supplementary Materials.

**Author Contributions:** Conceptualization, X.L. and Y.C. (Yong Cheng); methodology, X.L. and Q.X.; software, L.W.; validation, L.W. and Z.Z.; formal analysis, L.L.; investigation, Z.Z.; resources, X.L.; data curation, Y.C. (Yong Chen); writing—original draft preparation, Q.X.; writing—review and editing, X.L.; visualization, Y.C. (Yong Chen); supervision, Y.C. (Yong Cheng); project administration, L.L.; funding acquisition, X.L. All authors have read and agreed to the published version of the manuscript.

**Funding:** This work was supported by the National Natural Science Foundation of China (12164013, 51662004).

**Data Availability Statement:** Not applicable.

**Conflicts of Interest:** The authors declare that they have no known competing financial interests or personal relationships that could have appeared to influence the work reported in this paper.

## References

- Pan, H.; Shao, Y.; Yan, P.; Cheng, Y.; Han, K.S.; Nie, Z.; Wang, C.; Yang, J.; Li, X.; Bhattacharya, P.; et al. Reversible aqueous zinc/manganese oxide energy storage from conversion reactions. *Nat. Energy* **2016**, *1*, 16039. [[CrossRef](#)]
- Kundu, D.; Adams, B.D.; Duffort, V.; Vajargah, S.H.; Nazar, L.F. A high-capacity and long-life aqueous rechargeable zinc battery using a metal oxide intercalation cathode. *Nat. Energy* **2016**, *1*, 16119. [[CrossRef](#)]
- Huang, Y.; Chang, Z.; Liu, W.; Huang, W.; Dong, L.; Kang, F.; Xu, C. Layer-by-layer zinc metal anodes to achieve long-life zinc-ion batteries. *Chem. Eng. J.* **2022**, *431*, 133902. [[CrossRef](#)]
- Zeng, X.; Hao, J.; Wang, Z.; Mao, J.; Guo, Z. Recent progress and perspectives on aqueous Zn-based rechargeable batteries with mild aqueous electrolytes. *Energy Storage Mater.* **2019**, *20*, 410–437. [[CrossRef](#)]
- Li, H.; Yang, Q.; Mo, F.; Liang, G.; Liu, Z.; Tang, Z.; Ma, L.; Liu, J.; Shi, Z.; Zhi, C. MoS<sub>2</sub> nanosheets with expanded interlayer spacing for rechargeable aqueous Zn-ion batteries. *Energy Storage Mater.* **2019**, *19*, 94–101. [[CrossRef](#)]
- Liang, H.; Cao, Z.; Ming, F.; Zhang, W.; Anjum, D.H.; Cui, Y.; Cavallo, L.; Alshareef, H.N. Aqueous Zinc-Ion Storage in MoS<sub>2</sub> by Tuning the Intercalation Energy. *Nano Lett.* **2019**, *19*, 3199–3206. [[CrossRef](#)]
- Tansel, B. Significance of thermodynamic and physical characteristics on permeation of ions during membrane separation: Hydrated radius, hydration free energy and viscous effects. *Sep. Purif. Technol.* **2012**, *86*, 119–126. [[CrossRef](#)]
- Xia, C.; Guo, J.; Li, P.; Zhang, X.; Alshareef, H.N. Highly Stable Aqueous Zinc-Ion Storage Using a Layered Calcium Vanadium Oxide Bronze Cathode. *Angew. Chem. Int. Ed.* **2018**, *57*, 3943–3948. [[CrossRef](#)]
- Li, C.; Xie, X.; Liang, S.; Zhou, J. Issues and Future Perspective on Zinc Metal Anode for Rechargeable Aqueous Zinc-ion Batteries. *Energy Environ. Mater.* **2020**, *3*, 146–159. [[CrossRef](#)]
- Zhang, X.; Tang, Y.; He, P.; Zhang, Z.; Chen, T. Edge-rich vertical graphene nanosheets templating V<sub>2</sub>O<sub>5</sub> for highly durable zinc ion battery. *Carbon* **2021**, *172*, 207–213. [[CrossRef](#)]

11. Lee, W.S.V.; Xiong, T.; Wang, X.; Xue, J. Unraveling MoS<sub>2</sub> and Transition Metal Dichalcogenides as Functional Zinc-Ion Battery Cathode: A Perspective. *Small Methods* **2021**, *5*, 2000815. [[CrossRef](#)]
12. Sarkar, D.; Das, D.; Das, S.; Kumar, A.; Patil, S.; Nanda, K.K.; Sarma, D.D.; Shukla, A. Expanding Interlayer Spacing in MoS<sub>2</sub> for Realizing an Advanced Supercapacitor. *ACS Energy Lett.* **2019**, *4*, 1602–1609. [[CrossRef](#)]
13. Liu, X.; Zhang, G.; Zhang, Y.-W. Thermal conduction across the one-dimensional interface between a MoS<sub>2</sub> monolayer and metal electrode. *Nano Res.* **2016**, *9*, 2372–2383. [[CrossRef](#)]
14. Jin Jang, Y.; Park, S.-K. Rational design of hierarchical Ni-Mo bimetallic Selenide/N-doped carbon microspheres toward high-performance potassium ion batteries. *Appl. Surf. Sci.* **2022**, *583*, 152491. [[CrossRef](#)]
15. Zhao, C.; Yu, C.; Zhang, M.; Sun, Q.; Li, S.; Norouzi Banis, M.; Han, X.; Dong, Q.; Yang, J.; Wang, G.; et al. Enhanced sodium storage capability enabled by super wide-interlayer-spacing MoS<sub>2</sub> integrated on carbon fibers. *Nano Energy* **2017**, *41*, 66–74. [[CrossRef](#)]
16. Liu, W.; Hao, J.; Xu, C.; Mou, J.; Dong, L.; Jiang, F.; Kang, Z.; Wu, J.; Jiang, B.; Kang, F. Investigation of zinc ion storage of transition metal oxides, sulfides, and borides in zinc ion battery systems. *Chem. Commun.* **2017**, *53*, 6872–6874. [[CrossRef](#)]
17. Khan, M.F.; Miriyala, N.; Lee, J.; Hassanpourfard, M.; Kumar, A.; Thundat, T. Heat capacity measurements of sub-nanoliter volumes of liquids using bimaterial microchannel cantilevers. *Appl. Phys. Lett.* **2016**, *108*, 211906. [[CrossRef](#)]
18. Oh, H.G.; Park, S.-K. Co-MOF derived MoSe<sub>2</sub>@CoSe<sub>2</sub>/N-doped carbon nanorods as high-performance anode materials for potassium ion batteries. *Int. J. Energy Res.* **2022**, *46*, 10677–10688. [[CrossRef](#)]
19. Shao, F.; Huang, Y.; Wang, X.; Li, Z.; Huang, X.; Huang, W.; Dong, L.; Kang, F.; Liu, W.; Xu, C. MoS<sub>2</sub> with high 1T phase content enables fast reversible zinc-ion storage via pseudocapacitance. *Chem. Eng. J.* **2022**, *448*, 137688. [[CrossRef](#)]
20. Liu, J.; Gong, N.; Peng, W.; Li, Y.; Zhang, F.; Fan, X. Vertically aligned 1 T phase MoS<sub>2</sub> nanosheet array for high-performance rechargeable aqueous Zn-ion batteries. *Chem. Eng. J.* **2022**, *428*, 130981. [[CrossRef](#)]
21. Acerce, M.; Voiry, D.; Chhowalla, M. Metallic 1T phase MoS<sub>2</sub> nanosheets as supercapacitor electrode materials. *Nat. Nanotechnol.* **2015**, *10*, 313–318. [[CrossRef](#)]
22. Liu, F.; Li, L.; Xu, S.; Guo, J.; Ling, Y.; Zhang, Y.; Gong, W.; Wei, L.; Wang, C.; Zhang, Q.; et al. Cobalt-doped MoS<sub>2</sub>·nH<sub>2</sub>O nanosheets induced heterogeneous phases as high-rate capability and long-term cyclability cathodes for wearable zinc-ion batteries. *Energy Storage Mater.* **2023**, *55*, 1–11. [[CrossRef](#)]
23. Li, S.; Liu, Y.; Zhao, X.; Shen, Q.; Zhao, W.; Tan, Q.; Zhang, N.; Li, P.; Jiao, L.; Qu, X. Sandwich-Like Heterostructures of MoS<sub>2</sub>/Graphene with Enlarged Interlayer Spacing and Enhanced Hydrophilicity as High-Performance Cathodes for Aqueous Zinc-Ion Batteries. *Adv. Mater.* **2021**, *33*, 2007480. [[CrossRef](#)]
24. Li, S.; Liu, Y.; Zhao, X.; Cui, K.; Shen, Q.; Li, P.; Qu, X.; Jiao, L. Molecular Engineering on MoS<sub>2</sub> Enables Large Interlayers and Unlocked Basal Planes for High-Performance Aqueous Zn-Ion Storage. *Angew. Chem. Int. Ed.* **2021**, *60*, 20286–20293. [[CrossRef](#)]
25. Wang, S.; Zhang, D.; Li, B.; Zhang, C.; Du, Z.; Yin, H.; Bi, X.; Yang, S. Ultrastable In-Plane 1T-2H MoS<sub>2</sub> Heterostructures for Enhanced Hydrogen Evolution Reaction. *Adv. Energy Mater.* **2018**, *8*, 1801345. [[CrossRef](#)]
26. Huang, X.; Leng, M.; Xiao, W.; Li, M.; Ding, J.; Tan, T.L.; Lee, W.S.V.; Xue, J. Activating Basal Planes and S-Terminated Edges of MoS<sub>2</sub> toward More Efficient Hydrogen Evolution. *Adv. Funct. Mater.* **2017**, *27*, 1604943. [[CrossRef](#)]
27. Nipane, A.; Karmakar, D.; Kaushik, N.; Karande, S.; Lodha, S. Few-Layer MoS<sub>2</sub> p-Type Devices Enabled by Selective Doping Using Low Energy Phosphorus Implantation. *ACS Nano* **2016**, *10*, 2128–2137. [[CrossRef](#)]
28. Zhou, M.; Cheng, L.; Han, B.; Zhang, H.; Chen, J.; Xie, F.; Wang, N.; Jin, Y.; Meng, H. Cobalt-doped molybdenum disulfide with rich defects and extended layered structure for rechargeable zinc-ion batteries. *J. Alloy Compd.* **2022**, *916*, 165487. [[CrossRef](#)]
29. Hu, J.; Yuan, J.; Zhao, L.; Li, G.; Chen, D.; Han, W.; Chu, Y.; Cui, X.; Li, C.; Zhang, Y. Few-layered MoS<sub>2</sub> with S-vacancies anchored on N-doped carbon flower for high performance sodium storage. *J. Alloy Compd.* **2022**, *895*, 162514. [[CrossRef](#)]
30. Wang, X.; Zhang, Y.; Si, H.; Zhang, Q.; Wu, J.; Gao, L.; Wei, X.; Sun, Y.; Liao, Q.; Zhang, Z.; et al. Single-Atom Vacancy Defect to Trigger High-Efficiency Hydrogen Evolution of MoS<sub>2</sub>. *J. Am. Chem. Soc.* **2020**, *142*, 4298–4308. [[CrossRef](#)]
31. Xu, W.; Sun, C.; Zhao, K.; Cheng, X.; Rawal, S.; Xu, Y.; Wang, Y. Defect engineering activating (Boosting) zinc storage capacity of MoS<sub>2</sub>. *Energy Storage Mater.* **2019**, *16*, 527–534. [[CrossRef](#)]
32. Xie, J.; Zhang, J.; Li, S.; Grote, F.; Zhang, X.; Zhang, H.; Wang, R.; Lei, Y.; Pan, B.; Xie, Y. Controllable Disorder Engineering in Oxygen-Incorporated MoS<sub>2</sub> Ultrathin Nanosheets for Efficient Hydrogen Evolution. *J. Am. Chem. Soc.* **2013**, *135*, 17881–17888. [[CrossRef](#)]
33. Xie, J.; Zhang, H.; Li, S.; Wang, R.; Sun, X.; Zhou, M.; Zhou, J.; Lou, X.W.; Xie, Y. Defect-Rich MoS<sub>2</sub> Ultrathin Nanosheets with Additional Active Edge Sites for Enhanced Electrocatalytic Hydrogen Evolution. *Adv. Mater.* **2013**, *25*, 5807–5813. [[CrossRef](#)]
34. Wang, D.; Pan, Z.; Wu, Z.; Wang, Z.; Liu, Z. Hydrothermal synthesis of MoS<sub>2</sub> nanoflowers as highly efficient hydrogen evolution reaction catalysts. *J. Power Sources* **2014**, *264*, 229–234. [[CrossRef](#)]
35. Nguyen, T.P.; Kim, I.T. W<sub>2</sub>C/WS<sub>2</sub> Alloy Nanoflowers as Anode Materials for Lithium-Ion Storage. *Nanomaterials* **2020**, *10*, 1336. [[CrossRef](#)]
36. Song, H.; Li, T.; He, T.; Wang, Z.; Fang, D.; Wang, Y.; Li, X.L.; Zhang, D.; Hu, J.; Huang, S. Cooperative catalytic Mo-S-Co heterojunctions with sulfur vacancies for kinetically boosted lithium-sulfur battery. *Chem. Eng. J.* **2022**, *450*, 138115. [[CrossRef](#)]
37. Ma, D.; Li, Y.; Mi, H.; Luo, S.; Zhang, P.; Lin, Z.; Li, J.; Zhang, H. Robust SnO<sub>2-x</sub> Nanoparticle-Impregnated Carbon Nanofibers with Outstanding Electrochemical Performance for Advanced Sodium-Ion Batteries. *Angew. Chem. Int. Ed.* **2018**, *57*, 8901–8905. [[CrossRef](#)]

38. Leng, K.; Chen, Z.; Zhao, X.; Tang, W.; Tian, B.; Nai, C.T.; Zhou, W.; Loh, K.P. Phase Restructuring in Transition Metal Dichalcogenides for Highly Stable Energy Storage. *ACS Nano* **2016**, *10*, 9208–9215. [[CrossRef](#)]
39. Liu, H.; Su, D.; Zhou, R.; Sun, B.; Wang, G.; Qiao, S.Z. Highly Ordered Mesoporous MoS<sub>2</sub> with Expanded Spacing of the (002) Crystal Plane for Ultrafast Lithium Ion Storage. *Adv. Energy Mater.* **2012**, *2*, 970–975. [[CrossRef](#)]
40. Shi, S.; Sun, Z.; Hu, Y.H. Synthesis, stabilization and applications of 2-dimensional 1T metallic MoS<sub>2</sub>. *J. Mater. Chem. A* **2018**, *6*, 23932–23977. [[CrossRef](#)]
41. Guo, Y.; Sun, D.; Ouyang, B.; Raja, A.; Song, J.; Heinz, T.F.; Brus, L.E. Probing the Dynamics of the Metallic-to-Semiconducting Structural Phase Transformation in MoS<sub>2</sub> Crystals. *Nano Lett.* **2015**, *15*, 5081–5088. [[CrossRef](#)]
42. Fang, Y.; Pan, J.; He, J.; Luo, R.; Wang, D.; Che, X.; Bu, K.; Zhao, W.; Liu, P.; Mu, G.; et al. Structure Re-determination and Superconductivity Observation of Bulk 1T MoS<sub>2</sub>. *Angew. Chem. Int. Ed.* **2018**, *57*, 1232–1235. [[CrossRef](#)]
43. Yin, Y.; Han, J.; Zhang, Y.; Zhang, X.; Xu, P.; Yuan, Q.; Samad, L.; Wang, X.; Wang, Y.; Zhang, Z.; et al. Contributions of Phase, Sulfur Vacancies, and Edges to the Hydrogen Evolution Reaction Catalytic Activity of Porous Molybdenum Disulfide Nanosheets. *J. Am. Chem. Soc.* **2016**, *138*, 7965–7972. [[CrossRef](#)]
44. Xue, H.; Meng, A.; Chen, C.; Xue, H.; Li, Z.; Wang, C. Phosphorus-doped MoS<sub>2</sub> with sulfur vacancy defects for enhanced electrochemical water splitting. *Sci. China Mater.* **2022**, *65*, 712–720. [[CrossRef](#)]
45. Liu, H.; Wang, J.-G.; Hua, W.; You, Z.; Hou, Z.; Yang, J.; Wei, C.; Kang, F. Boosting zinc-ion intercalation in hydrated MoS<sub>2</sub> nanosheets toward substantially improved performance. *Energy Storage Mater.* **2021**, *35*, 731–738. [[CrossRef](#)]
46. Angamuthu, G.; Rengarajan, V. MoS<sub>2</sub> mediated nitrogen enriched composite material for high and fast Li-ion storage. *Appl. Surf. Sci.* **2020**, *525*, 146437. [[CrossRef](#)]
47. Sheng, Z.; Qi, P.; Lu, Y.; Liu, G.; Chen, M.; Gan, X.; Qin, Y.; Hao, K.; Tang, Y. Nitrogen-Doped Metallic MoS<sub>2</sub> Derived from a Metal–Organic Framework for Aqueous Rechargeable Zinc-Ion Batteries. *ACS Appl. Mater. Interfaces* **2021**, *13*, 34495–34506. [[CrossRef](#)]
48. Eda, G.; Yamaguchi, H.; Voiry, D.; Fujita, T.; Chen, M.; Chhowalla, M. Photoluminescence from Chemically Exfoliated MoS<sub>2</sub>. *Nano Lett.* **2011**, *11*, 5111–5116. [[CrossRef](#)]
49. Cho, J.; Ryu, S.; Gong, Y.J.; Pyo, S.; Yun, H.; Kim, H.; Lee, J.; Yoo, J.; Kim, Y.S. Nitrogen-doped MoS<sub>2</sub> as a catalytic sulfur host for lithium-sulfur batteries. *Chem. Eng. J.* **2022**, *439*, 135568. [[CrossRef](#)]
50. Liu, J.; Wang, Z.; Li, J.; Cao, L.; Lu, Z.; Zhu, D. Structure Engineering of MoS<sub>2</sub> via Simultaneous Oxygen and Phosphorus Incorporation for Improved Hydrogen Evolution. *Small* **2020**, *16*, 1905738. [[CrossRef](#)]
51. Wu, W.; Zhao, Y.; Li, S.; He, B.; Liu, H.; Zeng, X.; Zhang, J.; Wang, G. P doped MoS<sub>2</sub> nanoplates embedded in nitrogen doped carbon nanofibers as an efficient catalyst for hydrogen evolution reaction. *J. Colloid Interface Sci.* **2019**, *547*, 291–298. [[CrossRef](#)]
52. Chae, M.S.; Heo, J.W.; Lim, S.-C.; Hong, S.-T. Electrochemical Zinc-Ion Intercalation Properties and Crystal Structures of ZnMo<sub>6</sub>S<sub>8</sub> and Zn<sub>2</sub>Mo<sub>6</sub>S<sub>8</sub> Chevrel Phases in Aqueous Electrolytes. *Inorg. Chem.* **2016**, *55*, 3294–3301. [[CrossRef](#)]
53. Cheng, Y.; Luo, L.; Zhong, L.; Chen, J.; Li, B.; Wang, W.; Mao, S.X.; Wang, C.; Sprenkle, V.L.; Li, G.; et al. Highly Reversible Zinc-Ion Intercalation into Chevrel Phase Mo<sub>6</sub>S<sub>8</sub> Nanocubes and Applications for Advanced Zinc-Ion Batteries. *ACS Appl. Mater. Interfaces* **2016**, *8*, 13673–13677. [[CrossRef](#)]
54. Zhang, K.; Jin, B.; Gao, Y.; Zhang, S.; Shin, H.; Zeng, H.; Park, J.H. Aligned Heterointerface-Induced 1T-MoS<sub>2</sub> Monolayer with Near-Ideal Gibbs Free for Stable Hydrogen Evolution Reaction. *Small* **2019**, *15*, 1804903. [[CrossRef](#)]
55. Xu, J.; Dong, Z.; Huang, K.; Wang, L.; Wei, Z.; Yu, L.; Wu, X. Flexible design of large layer spacing V-MoS<sub>2</sub>@C cathode for high-energy zinc-ion battery storage. *Scr. Mater.* **2022**, *209*, 114368. [[CrossRef](#)]
56. He, P.; Yan, M.; Zhang, G.; Sun, R.; Chen, L.; An, Q.; Mai, L. Layered VS<sub>2</sub> Nanosheet-Based Aqueous Zn Ion Battery Cathode. *Adv. Energy Mater.* **2017**, *7*, 1601920. [[CrossRef](#)]
57. Augustyn, V.; Come, J.; Lowe, M.A.; Kim, J.W.; Taberna, P.-L.; Tolbert, S.H.; Abruna, H.D.; Simon, P.; Dunn, B. High-rate electrochemical energy storage through Li<sup>+</sup> intercalation pseudocapacitance. *Nat. Mater.* **2013**, *12*, 518–522. [[CrossRef](#)]
58. Augustyn, V.; Simon, P.; Dunn, B. Pseudocapacitive oxide materials for high-rate electrochemical energy storage. *Energy Environ. Sci.* **2014**, *7*, 1597–1614. [[CrossRef](#)]
59. Cai, C.; Tao, Z.; Zhu, Y.; Tan, Y.; Wang, A.; Zhou, H.; Yang, Y. A nano interlayer spacing and rich defect 1T-MoS<sub>2</sub> as cathode for superior performance aqueous zinc-ion batteries. *Nanoscale Adv.* **2021**, *3*, 3780–3787. [[CrossRef](#)]
60. Yao, J.; Jin, T.; Li, Y.; Xiao, S.; Huang, B.; Jiang, J. Electrochemical performance of Fe<sub>2</sub>(SO<sub>4</sub>)<sub>3</sub> as a novel anode material for lithium-ion batteries. *J. Alloy Compd.* **2021**, *886*, 161238. [[CrossRef](#)]
61. Yao, J.; Yang, Y.; Li, Y.; Jiang, J.; Xiao, S.; Yang, J. Interconnected  $\alpha$ -Fe<sub>2</sub>O<sub>3</sub> nanoparticles prepared from leaching liquor of tin ore tailings as anode materials for lithium-ion batteries. *J. Alloy Compd.* **2021**, *855*, 157288. [[CrossRef](#)]
62. Wu, T.; Zhu, K.; Qin, C.; Huang, K. Unraveling the role of structural water in bilayer V<sub>2</sub>O<sub>5</sub> during Zn<sup>2+</sup>-intercalation: Insights from DFT calculations. *J. Mater. Chem. A* **2019**, *7*, 5612–5620. [[CrossRef](#)]
63. Yan, M.; He, P.; Chen, Y.; Wang, S.; Wei, Q.; Zhao, K.; Xu, X.; An, Q.; Shuang, Y.; Shao, Y.; et al. Water-Lubricated Intercalation in V<sub>2</sub>O<sub>5</sub>·nH<sub>2</sub>O for High-Capacity and High-Rate Aqueous Rechargeable Zinc Batteries. *Adv. Mater.* **2018**, *30*, 1703725. [[CrossRef](#)]

64. Zhang, N.; Cheng, F.; Liu, Y.; Zhao, Q.; Lei, K.; Chen, C.; Liu, X.; Chen, J. Cation-Deficient Spinel  $ZnMn_2O_4$  Cathode in  $Zn(CF_3SO_3)_2$  Electrolyte for Rechargeable Aqueous Zn-Ion Battery. *J. Am. Chem. Soc.* **2016**, *138*, 12894–12901. [[CrossRef](#)]
65. Shaju, K.M.; Subba Rao, G.V.; Chowdari, B.V.R. Li ion kinetic studies on spinel cathodes,  $Li(M_{1/6}Mn_{11/6})O_4$  ( $M = Mn, Co, CoAl$ ) by GITT and EIS. *J. Mater. Chem.* **2003**, *13*, 106–113. [[CrossRef](#)]

**Disclaimer/Publisher's Note:** The statements, opinions and data contained in all publications are solely those of the individual author(s) and contributor(s) and not of MDPI and/or the editor(s). MDPI and/or the editor(s) disclaim responsibility for any injury to people or property resulting from any ideas, methods, instructions or products referred to in the content.